

# Weyl Fermions with various chiralities in a $f$ -electron ferromagnetic system: $\text{PrB}_4$

Dong-Choon Ryu<sup>1,2,3,\*</sup>, Junwon Kim<sup>1</sup>, Kyoo Kim<sup>4</sup>, Bongjae Kim<sup>2,6</sup>, Chang-Jong Kang<sup>3,5,†</sup> and B. I. Min<sup>1,‡</sup>

<sup>1</sup>*Department of Physics, Pohang University of Science and Technology, Pohang, 37673, Korea*

<sup>2</sup>*Department of Physics, Kunsan National University, Gunsan 54150, Korea*

<sup>3</sup>*Department of Physics, Chungnam National University, Daejeon 34134, Korea*

<sup>4</sup>*Korea Atomic Energy Research Institute, Daejeon, Korea*

<sup>5</sup>*Institute of Quantum Systems, Chungnam National University, Daejeon, 34134, Korea*

<sup>6</sup>*Department of Physics, Kyungpook National University, Daegu, 41566, Korea*

(Dated: September 9, 2024)

Rare-earth tetraborides ( $\text{RB}_4$ ) have attracted a lot of recent attention due to their intriguing electronic, magnetic, and topological properties. We have theoretically investigated topological properties of  $\text{PrB}_4$ , which is unique among  $\text{RB}_4$  family due to its ferromagnetic ground state. We have discovered that  $\text{PrB}_4$  is an intrinsic magnetic Weyl system possessing multiple topological band crossings with various chiral charges. Density-functional-theory band calculations combined with tight-binding band analysis reveal large Fermi-arc surface states, which are characteristic fingerprints of Weyl fermions. Anomalous Hall conductivity is estimated to be very large, ranging from 500 to  $1000 (\Omega \cdot \text{cm})^{-1}$  near the Fermi level, which also demonstrates the topological Weyl character of ferromagnetic  $\text{PrB}_4$ . These findings suggest that  $\text{PrB}_4$ , being a potential candidate of magnetic Weyl system, would be a promising rare-earth topological system for applications to next-generation spintronic and photonic devices.

## I. INTRODUCTION

Weyl semimetal is a topological system, which attracts a lot of recent attention in the condensed matter physics community [1–3]. A Weyl semimetal is featured by exotic bulk Weyl points of twofold-degenerate band crossings and the associated topological Fermi-arc surface states. Due to inherent chiral-anomaly nature of Weyl fermions, the Weyl system exhibits the negative longitudinal magnetoresistance. In addition, unusual phenomena of the chiral magnetic effect, the giant anomalous Hall effect, and the large magneto-optical Kerr effect are supposed to be realized in the Weyl systems as a consequence of the chiral anomaly [2–4]. The emergence of Weyl fermion excitation requires the breaking of either time-reversal ( $T$ ) or spatial inversion ( $P$ ) symmetry, because the existence of both symmetries produce the Kramers degenerate bands for all  $\mathbf{k}$ , and thereby any band crossing has fourfold degeneracy.

Since the pioneering study of Weyl semimetal on the  $T$ -breaking pyrochlore iridates [1], subsequent studies of Weyl systems have focused on  $P$ -breaking materials, and so most of reported Weyl systems belong to noncentrosymmetric crystals, such as transition-metal monophosphides and dichalcogenides [5–8]. In contrast,  $T$ -breaking magnetic Weyl systems (MWSs) are relatively less explored. Following earlier theoretical reports on the MWS candidates of  $\text{Y}_2\text{Ir}_2\text{O}_7$  [1],  $\text{HgCr}_2\text{Se}_4$  [9], and  $\text{SrRuO}_3$  [10], only a few more materials like  $\text{GdBiPt}$  [11, 12],  $\text{CeSb}$  [13], and  $\text{GdB}_4$  [14] have been proposed as MWS candidates. These systems, however, demand ma-

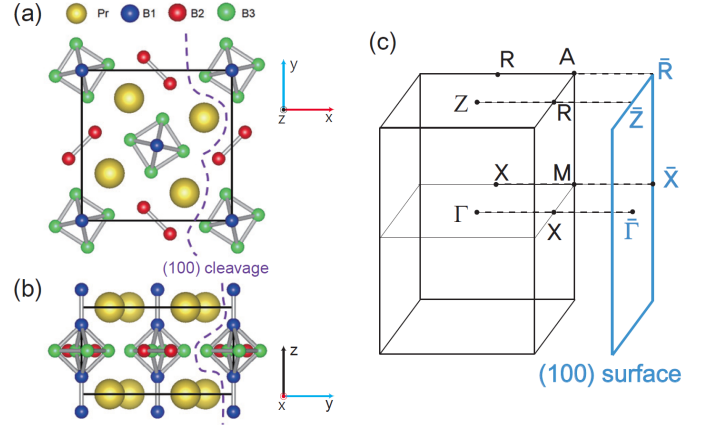


FIG. 1. (Color Online) Tetragonal crystal structure of  $\text{PrB}_4$  with nonsymmorphic  $P4/mbm$  space group. (a) top view and (b) side view. Purple dashed lines indicate (100) surface cleavage we have considered for the Pr-termination in Fig. 3. (c) Bulk and (100) surface BZ.

nipulation of the external magnetic  $B$ -field to generate Weyl points or to stabilize the magnetic ordering, and so experimental investigations were limited. Moreover, for  $\text{CeSb}$ , angle-resolved photoemission (ARPES) study raised a question about the existence of band inversion and the emergence of Weyl fermions [15].

More recently, Heusler-based  $\text{Co}_2\text{MnGa}$  [16, 17], Kagome-lattice-based  $\text{Mn}_3\text{Sn}$  [18] and  $\text{Co}_3\text{Sn}_2\text{S}_2$  [19, 20] were reported to be MWSs. In the cases of rare-earth systems,  $\text{PrAlGe}$ , in which both  $P$  and  $T$  are broken, was proposed to be an MWS candidate [21, 22]. Also,  $\text{EuB}_6$  was reported to be a candidate for a  $T$ -breaking MWS [23, 24]. Hence, there are only a number of genuine  $T$ -breaking MWS candidates, and they are mostly  $d$ -electron systems.

\* dcrhyu@postech.ac.kr

† Co-corresponding: cjkang87@cnu.ac.kr

‡ Co-corresponding: bimin@postech.ac.kr

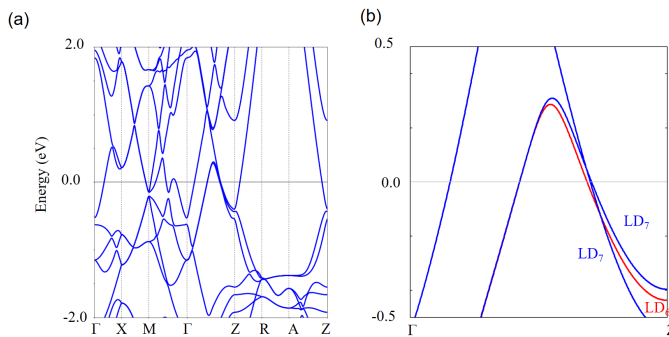


FIG. 2. (Color Online) (a) Bulk band structure of nonmagnetic  $\text{PrB}_4$  obtained by the  $4f$  open-core calculation, including the spin-orbit coupling. (b) Amplified band structure near  $E_F$  along  $\Gamma - Z$  with corresponding IRREP for each band. The band with the IRREP of  $\text{LD}_6$  is drawn in red for clarity.

In this work, we have investigated topological properties of a representative rare-earth tetraboride system,  $\text{PrB}_4$ , and found that  $\text{PrB}_4$  is a genuine  $T$ -breaking NWS with  $f$ -electrons. With its intrinsic ferromagnetism,  $\text{PrB}_4$  possesses unique Weyl fermion character with various types of chiral charges. Note that rare-earth tetraborides  $\text{RB}_4$  ( $R$ : rare-earth elements) exhibit diverse magnetic ground states, depending on  $R$  element, such as Kondo, ferromagnetic (FM), and antiferromagnetic (AFM) states. Furthermore, exotic topological properties were also predicted for tetraborides. As mentioned above,  $\text{GdB}_4$ , having the in-plane noncollinear AFM ground state of a well-known Shastry-Sutherland lattice type, was proposed to be a Weyl system in the presence of the external  $B$  field [14]. Albeit not  $\text{RB}_4$ , an actinide-tetraboride Kondo system,  $\text{PuB}_4$ , was reported to host intriguing fourfold-degenerate topological wallpaper fermions on its surface [25]. Similarly,  $\text{DyB}_4$ , which has the noncollinear AFM ground state, was reported to host magnetic wallpaper fermions [26].

$\text{PrB}_4$  is unique in that it is a sole ferromagnet among  $\text{RB}_4$ . According to a magnetic susceptibility experiment [27], upon cooling,  $\text{PrB}_4$  shows first the AFM ordering at  $T_N \sim 19.5$  K, and then the FM ordering below  $T_C \sim 15.9$  K. In view of the  $B$ -field-induced MWS for AFM  $\text{GdB}_4$ ,  $\text{PrB}_4$  in the FM phase is expected to have the Weyl-type band structure even in the absence of the external  $B$ -field. Indeed, for  $\text{PrB}_4$ , we have theoretically found that Weyl fermions with various chiral charges emerge in its FM ground state with associated topological Fermi-arc surface states. Also the estimated anomalous-Hall-conductivity (AHC), which originates from the large Berry curvature contributed by some Weyl nodes and band anticrossings, reaches as high as  $1000 (\Omega \cdot \text{cm})^{-1}$ , which corroborates that  $\text{PrB}_4$  is a new candidate of intrinsic rare-earth MWS.

## II. CRYSTAL STRUCTURE AND COMPUTATIONAL DETAILS

$\text{PrB}_4$  crystallizes in a tetragonal structure with the nonsymmorphic  $P4/mbm$  space group (SG 127). In Fig. 1, the crystal structure of  $\text{PrB}_4$  and its bulk and surface Brillouin zone (BZ) are depicted. The lattice constants and internal coordinates used in this study were adopted from the experiment ( $a=7.235$  Å,  $c=4.116$  Å) [28].

For the first-principles density functional theory (DFT) band calculations, we have employed the projector augmented wave (PAW) band method implemented in VASP in the generalized-gradient approximation (GGA) [29–31]. To describe the strongly-correlated Pr  $4f$  electrons, we have used the GGA+ $U$  calculations with Coulomb ( $U$ ) and exchange ( $J$ ) correlation parameters. We set the parameters for  $U = 4$  eV, which is a commonly accepted value for the Pr atom [32, 33], and  $J = 0.4$  eV, which reproduces well the observed magnetic moment of  $2.1 \mu_B$  per Pr atom [27] (see Fig. S1 in the supplement [34]).

Surface electronic structures and chiral charges of Weyl points are obtained based on a Wannierized tight-binding Hamiltonian [35] by utilizing the Wanniertools code [36]. We have also obtained the Berry curvature and estimated the anomalous Hall conductivity based on the Wannierized tight-binding bulk band structures.

## III. BULK BAND STRUCTURE OF NONMAGNETIC $\text{PrB}_4$

Figure 2(a) shows the bulk band structure of  $\text{PrB}_4$  obtained by the so-called “open-core” calculations, in which Pr  $4f$ -electrons are treated as core, so that the magnetism is suppressed. In Fig. 2(b), the amplified band structure near the Fermi level ( $E_F$ ) along  $\Gamma - Z$  is plotted with the irreducible representation (IRREP) of each band. Every band along  $\Gamma - Z$  is twofold-degenerate due to the time-reversal pairing, and so the fourfold-degenerate band crossing can occur when two bands of distinct IRREPs of  $\text{LD}_6$  and  $\text{LD}_7$  intersect, as shown in Fig. 2(b). Since the system preserves both the inversion  $P$  and time-reversal  $T$  symmetries in the absence of magnetism, any fourfold band crossing in this system must manifest itself as a Dirac point. Note that the Dirac point shown in Fig. 2(b) is of type-II nature. Surface states relevant to those Dirac points are further discussed in the supplement (Fig. S3) [34].

## IV. WEYL POINTS AND FERMI ARCS

Now we discuss the role of the magnetism in the emergence of the Weyl fermions in  $\text{PrB}_4$ . First, we have investigated energetics of three different magnetic structures of  $\text{PrB}_4$ , FM and two-types of AFM, and found that the

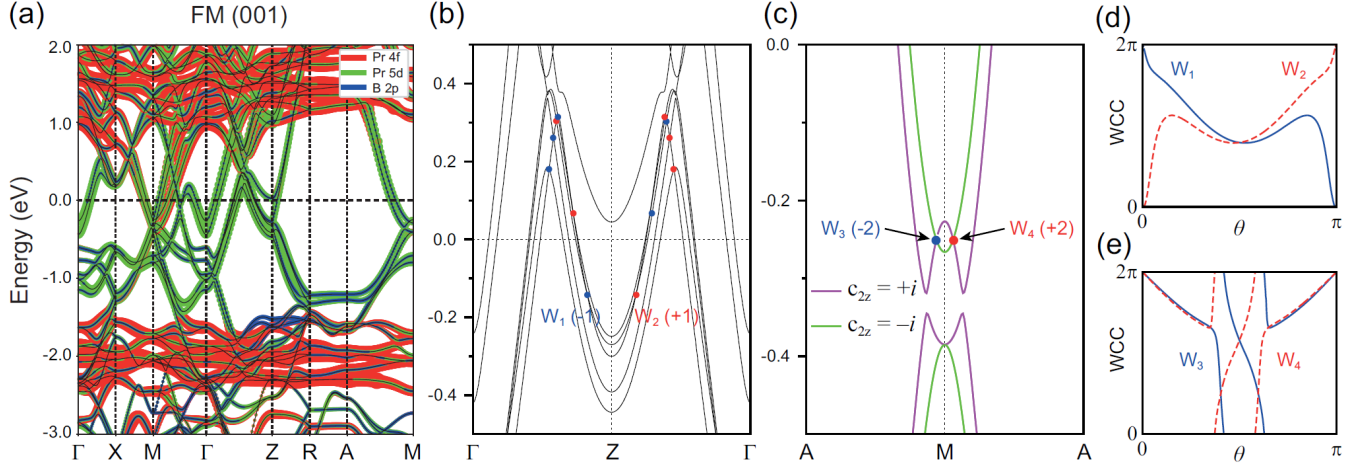


FIG. 3. (Color Online) (a) Bulk band structures of  $\text{PrB}_4$  with FM ordering along the (001) direction. (b), (c) Bulk band structures along rotationally invariant paths  $\Gamma - Z - \Gamma$  and  $A - M - A$  under the FM ordering. The Weyl points of topological band crossings are represented by red and blue dots, depending on their chiral charges. (d), (e) Evolution of Wannier charge center (WCC) on the spheres centered at four Weyl points  $W_1 - W_4$  marked in (b) and (c).

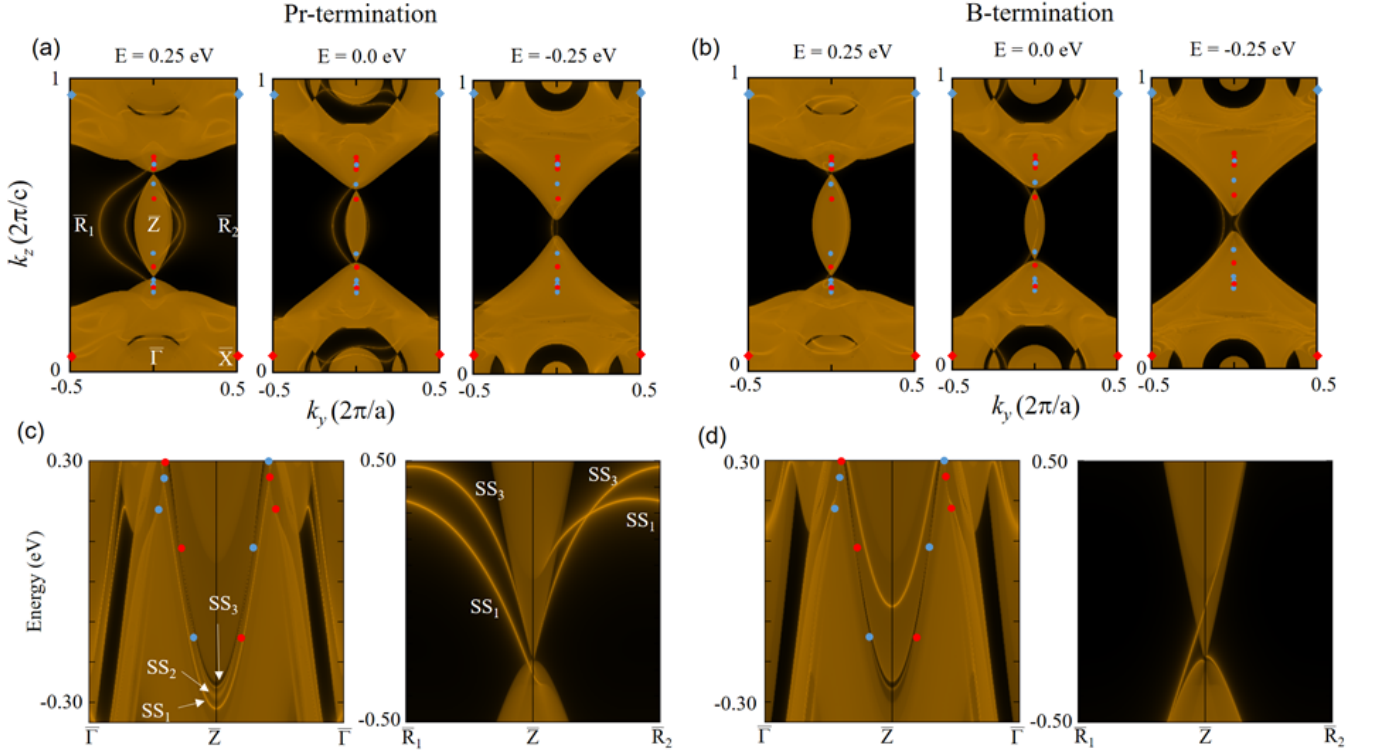


FIG. 4. (Color Online) Surface electronic structures on (100) surface of FM  $\text{PrB}_4$ . (a),(b) Constant-energy surfaces at various energy levels with Pr- and B-termination, respectively. Red and blue circles (diamonds) indicate the positions of Weyl fermions with chiralities  $\chi = \pm 1$  ( $\chi = \pm 2$ ), respectively. (c),(d) Surface band structures along  $\bar{\Gamma} - \bar{Z} - \bar{\Gamma}$  and  $\bar{R}_1 - \bar{Z} - \bar{R}_2$ . Red and blue dots denote the positions of Weyl points with positive and negative chiral charges, respectively.

FM state is indeed a ground state with magnetic ordering along the (001) direction, which is in agreement with the experimental results (see Fig. S2 and Table S1 in the supplement [34]). Then the formation of Weyl points, when breaking the time-reversal symmetry, is examined on the basis of the model Hamiltonian obtained from the non-

magnetic calculation by taking into account a Zeeman-like term (see Fig. S5 and S6 in the supplement [34]).

In order to examine the existence of Weyl points and their associated Fermi-arc surface states, we have investigated the band structures of FM  $\text{PrB}_4$  with (001) magnetic ordering. Figure 3(a) shows that Pr 4f states are

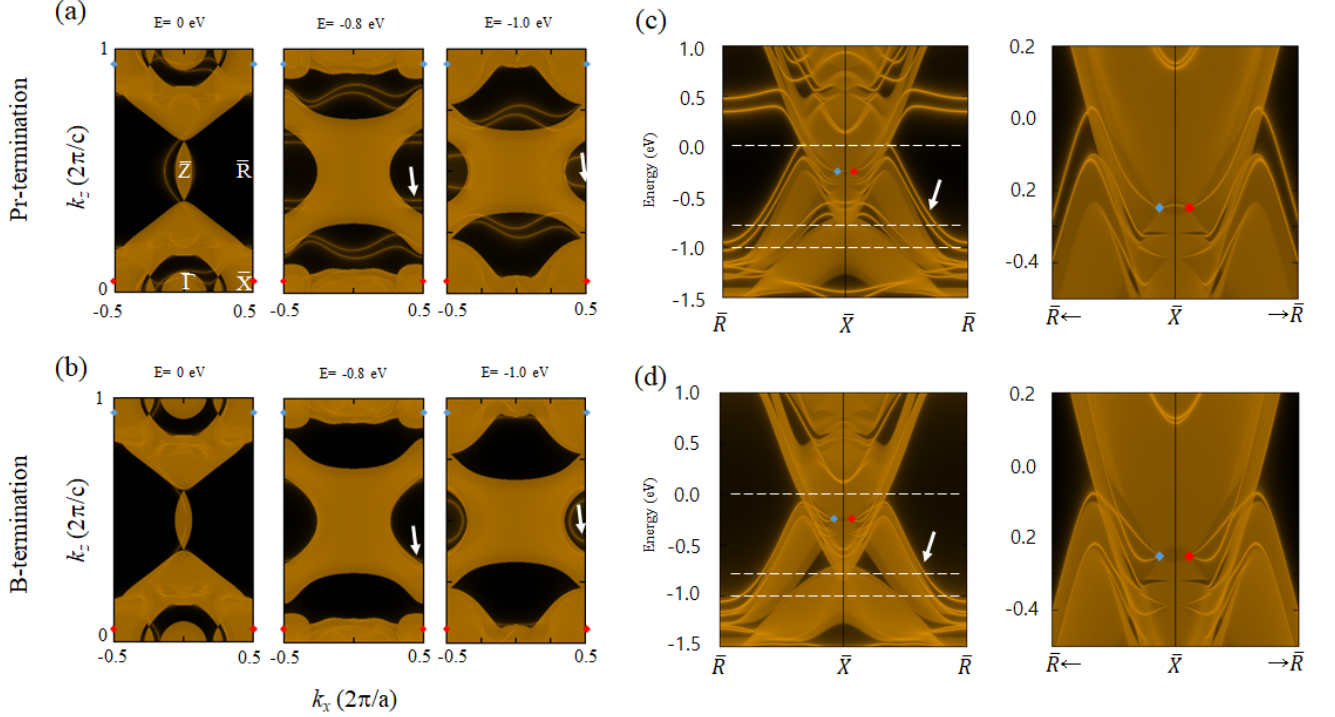


FIG. 5. (Color Online) (a), (b) Constant-energy surfaces at various energy levels, and (c), (d) surface band structures of the ferromagnetic phase of Weyl semimetallic PrB<sub>4</sub> for (top) Pr- and (bottom) B-termination. The rightmost figures correspond to the amplified plots of the left figures in (c) and (d). The positions of double Weyl fermions with chirality  $|\chi| = 2$  are denoted by red (positive) and blue (negative) diamonds in the figure. Surface Fermi-arc states connected to the double Weyl fermions are indicated by white arrows. The broken lines in (c) and (d) represent the energy levels of the constant-energy surfaces in (a) and (b).

located near  $-2$  eV and  $2$  eV, while wider Pr  $5d$  and B  $p$  bands are located near the Fermi level  $E_F$ .

The high symmetry  $k$ -paths, namely  $\Gamma-Z$  and  $M-A$ , are invariant under  $C_{4z}$  and  $C_{2z}$  rotations, as shown in Fig. 1, which leads to the occurrence of band crossings along those two paths. Indeed, the band crossings in the vicinity of  $E_F$  are clearly manifested in Figs. 3(b) and (c) along  $\Gamma-Z-\Gamma$  and  $A-M-A$  paths, respectively. The red and blue dots represent the Weyl points with positive and negative chiralities, respectively, which are identified from the Wilson loop calculations. There are several Weyl points along  $\Gamma-Z$ , while there is only one along  $A-M$  near  $E_F$  (see Table S2 in the supplement [34]).

Notable in Figs. 3(b) and (c) is that Weyl points on the  $\Gamma-Z$  path are conventional twofold-degenerate Weyl nodes, but those on the  $M-A$  path,  $W_3$  and  $W_4$ , are exotic fourfold-degenerate Weyl nodes, arising from the unique crystal symmetry of FM PrB<sub>4</sub>. Because of the magnetic ordering, the  $T$  symmetry is not preserved here, but the combination of  $T$  and nonsymmorphic screw-axis symmetry,  $S_y = \{C_{2y}|\frac{1}{2}\frac{1}{2}0\}$ , is preserved. Interestingly, this combined symmetry  $S_yT$  makes every band on the  $M-A$  path doubly degenerate even under the FM ordering. To be more specific, for any eigenstate

$\psi$  on  $M-A$ , there exists its Kramers pair  $S_yT\psi$  since  $(S_yT)^2 = \exp(ik_x) = -1$  on  $M-A$  (Note that both  $M$  and  $A$  have  $(k_x, k_y) = (\pi, \pi)$ ). Furthermore, when  $C_{2z}\psi = \pm i\psi$ , we have  $C_{2z}(S_yT\psi) = -\exp[i(k_x + k_y)]S_yTC_{2z}\psi = \pm i(S_yT\psi)$ . Namely, two bands in each Kramers pair have the same  $C_{2z}$  eigenvalues, which suggests that some accidental band crossings between two Kramers pairs with distinct  $C_{2z}$  eigenvalues can be preserved by crystal symmetry. In fact, the Wannier charge center (WCC) calculations in Figs. 3(d) and (e) confirmed that the chiralities (topological charges:  $\chi$ 's) of  $(W_1$  and  $W_2)$  and  $(W_3$  and  $W_4)$  Weyl points are  $\chi = \pm 1$  and  $\chi = \pm 2$ , implying the single-Weyl and double-Weyl points, respectively. The existence of both single- and double-Weyl points in PrB<sub>4</sub>, albeit somewhat complicated, would be more effective for applications to topological devices, as in the case of chiral fermion systems with multifold degeneracy [37, 38].

To confirm the Fermi arcs, which are one of the hallmarks of Weyl fermions, the surface electronic structure calculations were carried out. Although the (001) surface is the natural cleavage plane of PrB<sub>4</sub>, the (100) surface is more preferable to identify the Fermi arcs more clearly. On the (001) surface, all the Weyl points on  $\Gamma-Z$  and  $M-A$  are to be projected onto  $\bar{\Gamma}$  and  $\bar{M}$ , respectively.



This results in the overlap of Weyl points of opposite chiralities and, as a consequence, no vestige of the Fermi arcs. So we have examined the surface electronic structures on the (100) surface.

Figure 4 shows the two different sets of possible Fermi arcs depending on the surface terminations. In Fig. 4(a), which displays constant-energy surfaces for the Pr-termination, a few surface states presumed to be Fermi arcs are observed near  $\bar{Z}$ , and those Fermi arcs become larger for higher energy cut. In Fig. 4(c) are plotted surface band structures along  $\bar{\Gamma}-\bar{Z}-\bar{\Gamma}$  and  $\bar{R}-\bar{Z}-\bar{R}$ , in which three surface states  $SS_1-SS_3$  are identified. Comparative analysis of Fig. 4(a) and (c) suggests that  $SS_1$  corresponds to the largest Fermi arc shown in Fig. 4(a) connecting two charge-opposite Weyl points at higher energy, slightly below  $E = 0.3$  eV, while  $SS_2$  and  $SS_3$  connect four Weyl points close to  $\bar{Z}$ . On the other hand, for the B-termination of Fig. 4(b), putative Fermi arcs are buried in bulk Fermi surface near  $\bar{Z}$  and so are difficult to be discerned. Nevertheless, Figs. 4(b) and (d) reveal that there is a narrow band gap at  $\bar{Z}$  near  $E = -0.25$  eV, and Fermi arcs can be resolved in the gap region.

In contrast, the Fermi arcs arising from the Double Weyl points are difficult to identify, because they are mostly buried within the bulk continuum. Nevertheless, surface band structure and constant-energy surface calculations in Fig. 5 show that one of the long tails connected to those double Weyl points (indicated by white arrows in Fig. 5(c),(d)) is partially revealed between  $\bar{X}-\bar{R}$ . Indeed, the zoomed-in figures in (c) and (d) (the rightmost figures) of Fig. 5 clearly show the emergence of associated surface states from the double Weyl points, despite being buried within the bulk continuum.

It is worthwhile to compare the topological properties of  $\text{PrB}_4$  depending on its different magnetic states. As discussed earlier, we have shown that nonmagnetic  $\text{PrB}_4$  is a Dirac semimetal, hosting a type-II Dirac point along  $\Gamma-Z$ . For AFM  $\text{PrB}_4$ , we have found that it can be either a trivial normal metal (AFM1 configuration) or MWS (AFM2 configuration) depending on magnetic configurations, as demonstrated in Figs. S2 and S4 of the supplement [34]. However, the AFM2 MWS state does not host a Weyl point on  $\Gamma-Z$  nor does a double-Weyl point on  $M-A$ . Instead, it hosts Weyl points on generic  $k$ -points near  $M$  (see Table S3 in the supplement [34]). Notably,  $\text{PrB}_4$  exhibits a unique temperature-dependent variation in magnetic ordering upon cooling, transitioning from PM to AFM and finally to FM states. This leads to a topological phase transition from a topological Dirac semimetal to an intermediate AFM metal and, ultimately, to a magnetic Weyl semimetal as the temperature decreases. This property allows for the utilization of temperature-tuned topological properties in  $\text{PrB}_4$ .

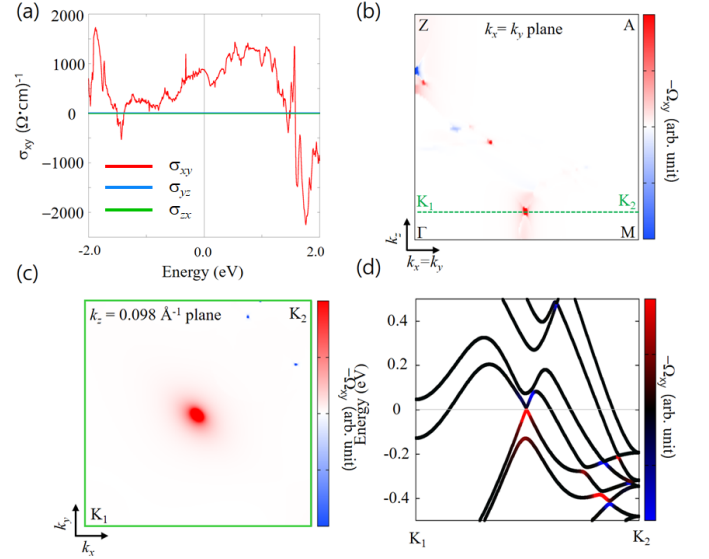


FIG. 6. (Color Online) (a) Chemical-potential energy dependent  $\sigma_{xy}$  for FM  $\text{PrB}_4$ . (b), (c) Berry curvature  $\Omega_{xy}(\mathbf{k})$  plot on  $k_x = k_y$  and  $k_z = 0.098 \text{ \AA}^{-1}$  planes at  $E_F$ , respectively.  $K_1$  and  $K_2$  are  $\mathbf{k}$ -points on the  $k_z = 0.098 \text{ \AA}^{-1}$  plane. (d) Band-resolved contribution to  $\Omega_{xy}(\mathbf{k})$  along the  $K_1-K_2$  path.

## V. ANOMALOUS HALL CONDUCTIVITY (AHC)

In MWSs, the AHC, which is much larger than the ordinary Hall conductivity, originates from intrinsic topological properties of the band structure, specifically the Berry curvature. We have estimated the AHC,  $\sigma_{\alpha\beta}$ , using the following equations [39]:

$$\sigma_{\alpha\beta} = -\frac{e^2}{\hbar} \int_{BZ} \frac{d\mathbf{k}}{(2\pi)^3} \Omega_{\alpha\beta}(\mathbf{k}), \quad (1)$$

where  $\Omega_{\alpha\beta}(\mathbf{k})$  is the total Berry curvature,

$$\Omega_{\alpha\beta}(\mathbf{k}) = -2Im \sum_v \sum_c \frac{v_{vc,\alpha}(\mathbf{k}) v_{cv,\beta}(\mathbf{k})}{[\epsilon_c(\mathbf{k}) - \epsilon_v(\mathbf{k})]^2}. \quad (2)$$

Here  $\epsilon_n(\mathbf{k})$  is the energy of  $n$ -th band at  $\mathbf{k}$ ,  $c$  and  $v$  denote unoccupied and occupied bands, and the velocity  $v_{nm,\alpha}(\mathbf{k})$  is given by

$$v_{nm,\alpha}(\mathbf{k}) = \langle \psi_{n\mathbf{k}} | \hat{v}_\alpha | \psi_{m\mathbf{k}} \rangle = \frac{1}{\hbar} \langle u_{n\mathbf{k}} | \frac{\partial \hat{H}(\mathbf{k})}{\partial k_\alpha} | u_{m\mathbf{k}} \rangle. \quad (3)$$

For FM state with magnetic ordering along (001) direction, the mirror symmetry  $M_z$  is present, which prohibits the  $\sigma_{yz}$  or  $\sigma_{zx}$  component, resulting in only  $\sigma_{xy}$  being finite.

In Fig. 6(a), we have shown the chemical-potential energy dependent AHC,  $\sigma_{xy}(E)$ , for FM  $\text{PrB}_4$ . The obtained  $\sigma_{xy}(E)$  is highly nonmonotonic with respect to energy position, and is very large ranging from 500

$\Omega^{-1}\text{cm}^{-1}$  to  $1000\ \Omega^{-1}\text{cm}^{-1}$  near  $E_F$  ( $E = 0$ ). The peaks and dips in the energy dependence of  $\sigma_{xy}(E)$  are expected to arise from the large Berry curvature at the corresponding energy. To explore the origin of such large AHC at  $E_F$ , we have examined Berry curvature  $\Omega_{xy}(\mathbf{k})$  on the two planes,  $k_x = k_y$  and  $k_z = 0.098\text{\AA}^{-1}$ . As plotted in Fig. 6(b) and (c), there are multiple sources of Berry curvature. Among them, those near  $\Gamma$ - $Z$  path in Fig. 6(b) are related to the Weyl points. According to Eq. (2), each Weyl point gives rise to huge AHC contribution, since  $\epsilon_c(\mathbf{k}) - \epsilon_v(\mathbf{k})$  goes to zero. However, since Weyl points are pair-created with opposite chirality, the sum of their Berry curvatures over the whole BZ would vanish.

Noteworthy is that large  $\Omega_{xy}(\mathbf{k})$  is observed near the center of  $\Gamma$ - $M$ , which becomes the largest near  $k_z = 0.098\text{\AA}^{-1}$  (Fig. 6(c)) would yield the large AHC. Indeed, band-resolved contribution to  $\Omega_{xy}(\mathbf{k})$  along  $K_1 - K_2$  in Fig. 6(d) clearly indicates that the large Berry curvature and AHC originate from the crossing-like band dispersion located inbetween  $K_1 - K_2$  near  $E_F$ . Significantly, a 10 meV gap is present there, implying an anticrossing feature in the band dispersion. Since this contribution does not arise from Weyl point, and any crystal symmetry  $g \in \{P, M_z, C_{4z}\}$  in  $\text{PrB}_4$  guarantees  $\Omega_{xy}(\mathbf{k}) = \Omega_{xy}(g\mathbf{k})$ , there is no cancellation in the total Berry curvature.

## VI. CONCLUDING REMARKS

We predict that a representative FM rare-earth tetraboride,  $\text{PrB}_4$ , hosts the multiple Weyl fermions with various topological charges, namely fourfold degenerate

double-Weyl point with charge  $\pm 2$  as well as conventional twofold degenerate Weyl point with charge  $\pm 1$ . Such a multitude of topological charges would facilitate  $\text{PrB}_4$  to be more advantageous than other MWSs having just conventional single-Weyl nodes, because one can explore the stronger topological effects, easier manipulability, and more stability, as in the case of the chiral fermion systems with multifold degeneracy. Furthermore, due to its unique temperature-dependent variation of magnetic ordering upon cooling, from paramagnetic (PM), AFM to FM, one can make use of temperature-tuned topological properties of  $\text{PrB}_4$ . Further experimental studies are encouraged to validate our theoretical predictions and extend our understanding of this fascinating material. Furthermore, our findings hold implications for exploring the topological properties of  $\text{ErB}_4$  and  $\text{TmB}_4$  since the AFM structures of  $\text{PrB}_4$  we investigated in this study are identical to those of  $\text{ErB}_4$  and  $\text{TmB}_4$  [40].

## Acknowledgments

Helpful discussions with J.-S. Kang are greatly appreciated. D.-C. R. and C.-J. K. were supported by NRF (Grant No. 2022R1C1C1008200) and the KISTI Supercomputing Center (Project No. KSC-2024-CRE-0050). D.-C. R. was supported by NRF (Grant No. RS-2023-00274550). C.-J. K. was also supported by the National Research Foundation of Korea Grant funded by the Korean Government (MOE). K. K. was supported by the internal R&D program at KAERI (No.524550-24). B.K. acknowledges support by NRF Grants (No. 2021R1C1C1007017 and No. 2022M3H4A1A04074153) and KISTI supercomputing Center (Project No. KSC-2022-CRE-0465).

- 
- [1] X. Wan, A. M. Turner, A. Vishwanath, and S. Y. Savrasov, *Phys. Rev. B* **83**, 205101 (2011).
  - [2] B. Yan and C. Felser, *Annu. Rev. Condens. Matter Phys.* **8**, 337 (2017), and references therein.
  - [3] N. P. Armitage, E. J. Mele, and A. Vishwanath, *Rev. Mod. Phys.* **90**, 015001 (2018), and references therein.
  - [4] N. P. Ong and S. Liang, *Nat. Rev. Phys.* **3**, 394 (2021), and references therein.
  - [5] H. Weng, C. Fang, Z. Fang, B. A. Bernevig, and X. Dai, *Phys. Rev. X* **5**, 011029 (2015).
  - [6] L. X. Yang, Z. K. Liu, Y. Sun, H. Peng, H. F. Yang, T. Zhang, B. Zhou, Y. Zhang, Y. F. Guo, M. Rahn, D. Prabhakaran, Z. Hussain, S.-K. Mo, C. Felser, B. Yan, Y. L. Chen, *Nat. Phys.* **11**, 728 (2015).
  - [7] A. A. Soluyanov, D. Gresch, A. Wang, Q. Wu, M. Troyer, X. Dai, and B. A. Bernevig, *Nature* **527**, 495 (2015).
  - [8] Y. Sun, S.-C. Wu, M. N. Ali, C. Felser, and B. Yan, *Phys. Rev. B* **92**, 161107(R) (2015).
  - [9] G. Xu, H. M. Weng, Z. J. Wang, X. Dai, and Z. Fang, *Phys. Rev. Lett.* **107**, 186806 (2011).
  - [10] Y. Chen, D. L. Bergman, and A. A. Burkov, *Phys. Rev. B* **88**, 125110 (2013).
  - [11] M. Hirschberger, S. Kushwaha, Z. Wang, Q. Gibson, S. Liang, C. A. Belvin, B. A. Bernevig, R. J. Cava, and N. P. Ong, *Nat. mater.* **15**, 1161 (2016).
  - [12] C. Shekhar, N. Kumar, V. Grinenko, S. Singh, R. Sarkar, H. Luetkens, S.-C. Wu, Y. Zhang, A. C. Komarek, E. Kampert, Y. Skourski, J. Wosnitza, W. Schnelle, A. McCollam, U. Zeitler, Jürgen Kübler, B. Yan, H.-H. Klauss, S. S. P. Parkin, and C. Felser, *PNAS* **115**, 9140 (2018).
  - [13] C. Guo, C. Cao, M. Smidman, F. Wu, Y. Zhang, F. Steglich, F.-C. Zhang, and H. Yuan, *npj Quantum materials* **2**, 39 (2017).
  - [14] W. Shon, D.-C. Ryu, K. Kim, B. I. Min, B. Kim, B. Kang, B. K. Cho, H.-J. Kim, J.-S. Rhyee, *Materials Today Physics* **11**, 100168 (2019).
  - [15] K. Kuroda, M. Ochi, H. S. Suzuki, M. Hirayama, M. Nakayama, R. Noguchi, C. Bareille, S. Akebi, S. Kunisada, T. Muro, M. D. Watson, H. Kitazawa, Y. Haga, T. K. Kim, M. Hoesch, S. Shin, R. Arita, and Takeshi Kondo, *Phys. Rev. Lett.* **120**, 086402 (2018).
  - [16] Z. Wang, M. G. Vergniory, S. Kushwaha, M. Hirschberger, E. V. Chulkov, A. Ernst, N. P. Ong, R. J. Cava, and B. A. Bernevig, *Phys. Rev. Lett.* **117**, 236401 (2017).

- (2016).
- [17] I. Belopolski, K. Manna, D. S. Sanchez, G. Chang, B. Ernst, J. Yin, S. S. Zhang, T. Cochran, N. Shumiya, H. Zheng, B. Singh, G. Bian, D. Multer, M. Litskevich, X. Zhou, S. -M. Huang, B. Wang, T. -R. Chang, S. -Y. Xu, A. Bansil, C. Felser, H. Lin, and M. Z. Hasan, *Science* **365**, 1278 (2019).
  - [18] K. Kuroda, T. Tomita, M. T. Suzuki, C. Bareille, A. A. Nugroho, P. Goswami, M. Ochi, M. Ikhlas, M. Nakayama, S. Akebi, R. Noguchi, R. Ishii, N. Inami, K. Ono, H. Kumigashira, A. Varykhalov, T. Muro, T. Koretune, R. Arita, S. Shin, T. Kondo, and S. Nakatsuji, *Nat. Mater.* **16**, 1090 (2017).
  - [19] D. F. Liu, A. J. Liang, E. K. Liu, Q. N. Xu, Y. W. Li, C. Chen, D. Pei, W. J. Shi, S. K. Mo4, P. Dudin, T. Kim, C. Cacho, G. Li, Y. Sun, L. X. Yang, Z. K. Liu, S. S. P. Parkin, C. Felser, and Y. L. Chen, *Science* **365**, 1282 (2019).
  - [20] N. Morali, R. Batabyal, P. K. Nag, E. Liu, Q. Xu, Y. Sun, B. Yan, C. Felser, N. Avraham, and H. Beidenkopf, *Science* **365**, 1286 (2019).
  - [21] G. Chang, B. Singh, S. -Y. Xu, G. Bian, S. -M. Huang, C. -H. Hsu, I. Belopolski, N. Alidoust, D. S. Sanchez, H. Zheng, H. Lu, X. Zhang, Y. Bian, T. -R. Chang, H. -T. Jeng, A. Bansil, H. Hsu, S. Jia, T. Neupert, H. Lin, and M. Z. Hasan, *Phys. Rev. B* **79**, 041104(R) (2018).
  - [22] D. S. Sanchez, G. Chang, I. Belopolski, H. Lu, J. -X. Yin, N. Alidoust, X. Xu, T. A. Cochran, X. Zhang, Y. Bian, S. S. Zhang, Y. -Y. Liu, J. Ma, G. Bian, H. Lin, S. -Y. Xu, S. Jia, and M. Z. Hasan, *Nat. commun.* **11**, 3356 (2020).
  - [23] S. Nie, Y. Sun, F.B. Prinz, Z. Wang, H. Weng, Z. Fang, X. Dai, *Phys. Rev. Lett.* **124** 076403 (2020)
  - [24] J. Yuan, X. Shi, H. Su, X. Zhang, X. Wang, N. Yu, Z. Zou, W. Zhao, J. Liu, Y. Guo, *Phys. Rev. B* **106** 054411 (2022)
  - [25] D. -C. Ryu, J. Kim, H. C. Choi, B. I. Min *J. Am. Chem. Soc.* **142**, 19278 (2020).
  - [26] Y. Hwang, Y. Qian, J. Kang, J. Lee, D. -C. Ryu, H. C. Choi, B. -J. Yang, *npj Comput. Mater.* **9**, 65 (2023).
  - [27] G. A. Wigger, E. Felder, R. Monnier, H.R. Ott, L. Pham, and Z. Fisk, *Phys. Rev. B* **72**, 014419 (2005).
  - [28] J. Etourneau, J.P. Mercurio, A. Berrada, P. Hagenmuller, *Journal of Less-Common Metals*, **67**, 531, (1979).
  - [29] G. Kresse and D. Joubert, *Phys. Rev. B* **59**, 1758 (1999).
  - [30] G. Kresse and J. Furthmüller, *Phys. Rev. B* **54**, 11169 (1996); *Comput. Mater. Sci.* **6**, 15 (1996).
  - [31] J. P. Perdew, K. Burke, and M. Ernzerhof, *Phys. Rev. Lett.* **77**, 3865 (1996).
  - [32] H. C. Choi, A. Laref, J. H. Shim, S. K. Kwon, and B. I. Min, *Journal of Applied Physics* **105**, 07E107 (2009).
  - [33] D. Destraz, L. Das, S. S. Tsirkin, Y. Xu, T. Neupert, J. Chang, A. Schilling, A. G. Grushin, J. Kohlbrecher, L. Keller, P. Puphal, E. Pomjakushina, and J. S. White, *npj Quantum Mater.* **5**, 5 (2020).
  - [34] See the Supplementary Material for (i) total energy calculations for different magnetic structures of PrB<sub>4</sub>, (ii) calculated spin and orbital magnetic moments of PrB<sub>4</sub> for different *J* values, (iii) Surface electronic structures of nonmagnetic phase of PrB<sub>4</sub>, (iv) Band structures of PrB<sub>4</sub> with antiferromagnetic orderings, and (v) Effect of a Zeeman-like term in the nonmagnetic open-core calculation.
  - [35] A. A. Mostofi, J. R. Yates, G. Pizzi, Y. S. Lee, I. Souza, D. Vanderbilt, N. Marzari, *Comput. Phys. Commun.* **185**, 2309 (2014).
  - [36] Q. S. Wu, S. N. Zhang, H.-F. Song, M. Troyer, and A. A. Soluyanov, *Comput. Phys. Commun.* **224**, 405 (2018).
  - [37] G. Chang, S.-Y. Xu, B.J. Wieder, D. S. Sanchez, S.-M. Huang, I. Belopolski, T.-R. Chang, S. Zhang, A. Bansil, H. Lin, and M. Z. Hasan, *Phys. Rev. Lett.* **119**, 206401 (2017).
  - [38] M. Z. Hasan, G. Chang, I. Belopolski, G. Bian, S.-Y. Xu, and J.-X. Yin, *Nat Rev Mater* **6**, 784 (2021).
  - [39] X. Wang, J. R. Yates, I. Souza, and D. Vanderbilt, *Phys. Rev. B* **74**, 195118 (2006).
  - [40] L. Ye, T. Suzuki, and J. G. Checkelsky *Phys. Rev. B* **95**, 174405 (2017).